Parametric study of coaxial dielectric barrier discharge in atmospheric pressure argon

Cite as: Phys. Plasmas **28**, 113505 (2021); https://doi.org/10.1063/5.0064574
Submitted: 24 July 2021 • Accepted: 03 November 2021 • Published Online: 24 November 2021

Hui Li, Chengxun Yuan, Anatoly Kudryavtsev, et al.

Physics of Plasmas ARTICLE scitation.org/journal/php

Parametric study of coaxial dielectric barrier discharge in atmospheric pressure argon

Cite as: Phys. Plasmas **28**, 113505 (2021); doi: 10.1063/5.0064574
Submitted: 24 July 2021 · Accepted: 3 November 2021 ·
Published Online: 24 November 2021

Hui Li,[1] Chengxun Yuan,[2] Anatoly Kudryavtsev,[2,3] T. Yasar Katircioglu,[4] and Ismail Rafatov[5,a)]

AFFILIATIONS

[1]National Key Laboratory of Electromagnetic Environment (LEME), China Research Institute of Radio Wave Propagation, Qingdao 266109, China
[2]School of Physics, Harbin Institute of Technology, Harbin 150001, Heilongjiang, People's Republic of China
[3]Saint Petersburg State University, 199034 St. Petersburg, Russia
[4]ARTECS Inc., A.U. Teknokent, 06830 Ankara, Turkey
[5]Department of Physics, Middle East Technical University, 06800 Ankara, Turkey

[a)]**Author to whom correspondence should be addressed:** rafatov@metu.edu.tr

ABSTRACT

A parametric study of the characteristics of coaxial dielectric barrier discharge sustained in atmospheric pressure argon is carried out. The numerical model is based on the drift-diffusion theory of gas discharges. The integral characteristics of the discharge, such as the root mean square of the discharge current, the period average dissipated power, and the efficiency of the power deposition, are explored in the parameter space spanned by the voltage amplitude and frequency of the applied AC field, the barrier dielectric constant, and the gas gap width.

I. INTRODUCTION

The possibility of utilization of dielectric barrier discharges (DBDs) as reliable sources of low temperature plasma at atmospheric pressure has led to a variety of industrial applications.[1] These applications include ozone generation, vapor deposition, surface modification, pollution control, excitation of CO lasers, flat plasma panels, excimer lamps, plasma medicine, and methane conversion.[1–4] The effective use of barrier discharges as sources of plasma for these applications depends mainly on the ability to control the plasma properties in these devices. This implies knowledge of the dependence of the discharge plasma characteristics on the external factors, such as the voltage and frequency of the applied AC field, chemical composition, pressure and flow rate of the working gas, and design of the discharge cell. Such knowledge can be obtained from the numerical modeling of the processes occurring in barrier discharges.

Barrier discharges can operate in a wide variety of conditions, which encompass gas pressures ranging from several tens of Torr to atmospheric pressure, gas gap widths ranging from fractions of a millimeter to several millimeters, voltage amplitudes ranging from hundreds of volts to several kilovolts, and field frequencies ranging from tens to several hundreds of kilohertz. The general properties of DBDs are reviewed and discussed in Refs. 1 and 5–8. Studies investigating the effect of discharge conditions (such as applied voltage parameters, gas gap width, electrode parameters, and material and width of the dielectric barrier) on the performance of the atmospheric pressure DBDs were carried out

- *for parallel-plate electrode configuration* numerically in Refs. 9 and 10 for He, in Ref. 11 for He/O_2 and Ar/O_2 mixtures, and
- *for coaxial electrode configuration* experimentally for Ar in Ref. 12 and numerically for He in Ref. 13 and for He/N mixture in Ref. 14.

Analysis for atmospheric pressure DBD based on an "electrical model," in which a real discharge cell is replaced with an equivalent electrical circuit, was performed in Ref. 15 for Ar and in Ref. 16 for He. Considerable computational and experimental efforts have been devoted to improve the energy efficiency and optimization of the DBD-based process of CO_2 conversion (see, e.g., Refs. 17 and 18 and references therein). There has been no comprehensive parametric study of coaxial DBDs in atmospheric pressure argon, based on a reliable numerical model. This work intends to fill this gap in the existing literature.

Coaxial dielectric barrier discharges in atmospheric pressure argon were studied experimentally and numerically in our previous work.[19] More precisely, the numerical model for barrier discharge

sustained in argon was validated and verified by superimposing the computed and measured data.[19] The model implemented in Ref. 19 is based on the fluid model for plasma, where the particle fluxes are expressed in the drift-diffusion form.[20,21] The electron kinetic coefficients (the electron transport coefficients as well as the rate constants of the electron induced elementary processes) are determined as functions of the mean electron energy. These data are derived by convolving the electron collision cross sections with electron energy distribution function (eedf), obtained from the solution to the electron Boltzmann equation. Alongside with this model, the model based on the Maxwellian eedf for electron kinetics as well as the model including the heat conduction equation for argon gas were employed in Ref. 19.

The present work is a further development of the study carried out in Ref. 19. It is aimed at the parametric study of the characteristics of DBDs in atmospheric pressure argon. The analysis is carried out over a parameter space spanned by the voltage amplitude and frequency of the applied AC field, the barrier dielectric constant, and the discharge gap width. The numerical model is similar to that in Ref. 19.

The analysis in Ref. 19 has revealed that attempts to fit the temporal behavior of the barrier discharge characteristics, such as experimentally observed current waveforms, due to a very erratic/irregular behavior of the discharge (which, in reality, represents a set of random electrical breakdowns), has not much sense, especially, when one takes into account that the model is spatially one-dimensional, while the phenomena is inherently three-dimensional. As observed experimentally,[19] after ignition the discharge did not occupy the entire cell, but a certain part of it. Moreover, the region of discharge initiation was arbitrary and uncontrollable. In fact, for a particular parameter regime, by tuning certain parameters in the model (such as secondary electron emission coefficient and settings for boundary conditions, which are the main sources of uncertainty in fluid models of gas discharges), in principle, it is possible to fit the discharge current waveform. However, for a different parameter regime, selected tuning parameters will not work. Therefore, in the present work, our analysis is especially directed at the parameter dependence of the integral characteristics of barrier discharge, such as time-average and root mean square (RMS) values of the discharge parameters. In fact, this approach is preferable to that based on the instantaneous values of these parameters. The point is that the integral characteristics eliminate the random/noise effects, while preserving global discharge properties.

In this paper, the equations and boundary conditions of the model, the plasma composition, the set of elementary processes, and the parameter regime are described in Sec. II. The parameter dependence of the RMS of the discharge current, the period average dissipated power, and efficiency of the power deposition are explored and discussed in Sec. III. Finally, the conclusions are presented in Sec. IV.

II. GAS DISCHARGE MODEL

Spatially one-dimensional axisymmetric fluid model (accounting for the radial coordinate) is applied to simulate the coaxial DBD plasma reactor. COMSOL Multiphysics 5.6[22] computational package with Plasma Module is employed. Schematic of the discharge tube cross section is illustrated in Fig. 1.

A. Governing equations

The gas discharge model includes particle balance equations

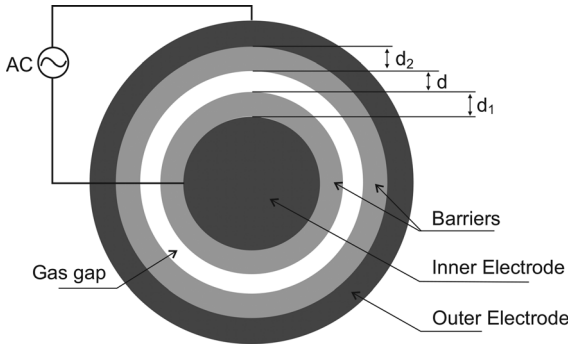

FIG. 1. Schematic description of coaxial DBD tube. Widths of dielectric layers are defined equal to $d_1 = 1.05$ mm and $d_2 = 1.175$ mm, similar to those in the barrier discharge cell in Ref. 19. The gas gap width d is varied from 0.5 to 4 mm.

$$\frac{\partial n_k}{\partial t} + \nabla \cdot \mathbf{\Gamma}_k = S_k, \tag{1}$$

where particle flux densities are approximated by the drift and diffusion terms given by

$$\mathbf{\Gamma}_k = \mathrm{sgn}(q_k)\mu_k n_k \mathbf{E} - D_k \nabla n_k, \tag{2}$$

the Poisson equation for the electrostatic field given by

$$-\varepsilon_0 \nabla^2 \varphi = \sum_k q_k n_k, \tag{3}$$

the energy balance equation for the electrons given by

$$\frac{\partial n_\varepsilon}{\partial t} + \nabla \cdot \mathbf{\Gamma}_\varepsilon = \mathbf{J}_e \cdot \mathbf{E} - Q_{el} - \sum_j \Delta E_j R_j, \tag{4}$$

and the energy balance equation for the background gas given by

$$c_p \frac{\partial}{\partial t}(\rho T_g) - \nabla \cdot \lambda \nabla T_g = \mathbf{J}_i \cdot \mathbf{E} + Q_{el}. \tag{5}$$

In these equations, φ and $\mathbf{E} = -\nabla\varphi$ are the electric potential and field, respectively; n stands for the particle number density; μ and D are the mobility and diffusion coefficients, respectively; q is the particle charge; and the subscript k defines the type of species. In the electron energy equation, $n_\varepsilon = n_e\bar{\varepsilon}$ is the electron energy density, $\bar{\varepsilon} = (3/2)k_B T_e$ is the mean electron energy, $\mathbf{J}_e = -e\mathbf{\Gamma}_e$ is the electron current density,

$$Q_{el} = \frac{3}{2}\frac{m_e}{m_g}\nu_{ea} n_e k_B (T_e - T_g)$$

accounts for the loss of electron energy in elastic collisions, ν_{ea} is the frequency of the electron-atomic elastic collisions, R_j is the rate of the jth reaction and ΔE_j is the corresponding energy loss (or gain), m is the particle mass, T is the kinetic temperature, and $\mathbf{\Gamma}_\varepsilon$ is the electron energy flux density given by

$$\mathbf{\Gamma}_\varepsilon = -D_\varepsilon \nabla n_\varepsilon - \mu_\varepsilon \mathbf{E} n_\varepsilon, \tag{6}$$

where the electron energy transport coefficients are related to the electron transport coefficients via $D_\varepsilon = 5/3 D_e$ and $\mu_\varepsilon = 5/3\mu_e$.[20] In the energy balance equation given by Eq. (5) for the background gas, c_p

denotes the specific heat at constant pressure, λ is the thermal conductivity, ρ is the mass density, and $\mathbf{J}_i = e\mathbf{\Gamma}_i$ is the total ion current density.

B. Plasma-chemical model

Calculations are performed for the barrier discharge in argon gas. Plasma-chemical model follows basically Ref. 23 and is identical to that in Ref. 19. Nine plasma species, viz., electrons, Ar atoms in ground state, three effective excited atomic levels (Ar^*, Ar_r^*, Ar^{**}), two excimer levels (Ar_2^*, Ar_2^{**}), and three sorts of ions (Ar^+, Ar_2^+, Ar_3^+) are taken into account (see Table I). The set of elementary processes is listed in Table II.

In the case of high pressure discharge, charge-transfer reactions are effective. By the reaction R18 (see Table II), atomic ions Ar^+ are rapidly converted into molecular dimeric ions Ar_2^+, and since the fraction of atomic ions in plasma becomes relatively small, dimeric ions prevail. The latter die in the dissociative recombination reaction R16. Trimeric ions Ar_3^+ are formed in the reaction R19 of conversion of molecular dimeric ions Ar_2^+. Dominance of trimeric ions would be expected, but Ar_3^+ ions have a lower dissociation energy and, therefore, quickly dissociate into dimeric ions via the reaction R20, and also recombine via the dissociative recombination R17. Consequently, the concentration of trimeric ions in plasma, as also confirmed by calculations, is approximately of the same order of magnitude as the concentration of dimeric ions.

The source terms S_k in the particle balance equations given by Eq. (1) are defined by the plasma-chemical reactions in the bulk of the discharge as follows:

$$S_k = \sum_i R_i - \sum_j R'_j, \tag{7}$$

where R_i and R'_j stand for the creation and destruction rates of kth species in ith and jth reactions, respectively. These are proportional to the rate constants and number densities of plasma species involved in the corresponding reactions.

The electron kinetic coefficients, namely, the electron transport (mobility and diffusion) coefficients as well as the rate constants of the electron-induced reactions, are determined as functions of the mean electron energy. These data are derived from eedf, obtained from the solution of the relevant electron Boltzmann equation.[20] Profiles of the electron collision cross sections vs the electron energy are shown in Fig. 2.

C. Boundary conditions

The boundary conditions are listed in Table III.[24,25] In these equations, $v_k = \sqrt{8k_B T_k/\pi m_k}$ defines the thermal velocity of the kth species. Switching parameter $a = 1$ if the direction of the electric field is toward the boundary; otherwise, $a = 0$. The secondary electron emission coefficient γ_i is defined equal to 0.1, the same on both dielectric surfaces and for all ionic components. In the electron energy boundary flux, the mean energy of secondary electrons ε_i is set equal to 2.5 V. In the boundary condition for the ionic flux densities $\xi_i = \gamma_f/(1 - 0.5\gamma_f)$, where the forward sticking coefficient $\gamma_f = 0.05$. The current density in the boundary conditions for the surface charge density σ is determined from $\mathbf{J}_g = \sum_k q_k \mathbf{\Gamma}_k$. The electric potential φ is continuous across the interfaces between the dielectric barrier and gas gap; on the ground electrode $\varphi = 0$ and $\varphi = V_0 \cos(2\pi ft)$ on the powered electrode, where f stands for the applied field frequency.

D. Parameter regime

The pressure of the argon gas is specified as atmospheric, $p = 760$ Torr. A parametric study of the discharge characteristics is carried out for the AC field frequency f ranging from 20 to 100 kHz, the amplitude of the applied voltage V_0 ranging from 0.8 to 4 kV, the barrier dielectric constant ε_r ranging from 4 to 8, and the gas gap width d ranging from 0.5 to 4 mm. These values cover the typical coaxial barrier discharge parameters used in experiments. The remaining input parameters are defined in the same manner as in the DBD cell studied experimentally and numerically in our previous work.[19] These are the outer radius of 4 mm of the inner quartz tube and its thickness $d_1 = 1.05$ mm, and the thickness $d_2 = 1.175$ mm of the outer quartz tube (see the schematic in Fig. 1). We also use in the calculations the values of the gas gap $d = 0.825$ mm and the barrier dielectric constant $\varepsilon_r = 4$ from Ref. 19 as reference parameters.

III. RESULTS AND DISCUSSIONS

A. Effect of the field frequency

Profiles of the RMS of the discharge current I_{rms} (a), the period average value of the dissipated power $\langle P_d \rangle$ (b), and efficiency η of the

TABLE I. List of argon species considered in the model.

Index	Species	Energy level (eV)	Effective level components
1	Ar	0	$2p^1S_0$
2	Ar^*	11.578	$4s[3/2]_2$, $4s'[1/2]_0$
3	Ar_r^*	11.726	$4s[3/2]_1$, $4s[1/2]_1$
4	Ar^{**}	13.171	$4p[1/2]_1$, $4p[5/2]_3$, $4p[5/2]_2$, $4p[3/2]_1$, $4p[3/2]_2$, $4p[1/2]_0$, $4p'[3/2]_1$, $4p'[3/2]_2$, $4p'[1/2]_1$, $4p'[1/2]_0$
5	Ar_2^*	12.2	$Ar_2(^3\sum_u^+)$, $Ar_2(^1\sum_u^+)$
6	Ar_2^{**}	13.42	Combination of divergent and weakly bound states
7	Ar^+	15.76	Ar^+ (ground state)
8	Ar_2^+	14.53	Ar_2^+ (ground state)
9	Ar_3^+	14.33	Ar_3^+ (ground state)

TABLE II. List of collision processes considered in the reaction kinetic model. The cross sections for de-excitation were obtained according to the principle of detailed balance.

Index	Reaction	Reaction rate constant
Elastic electron collision		
R1	$e + \mathrm{Ar} \rightarrow e + \mathrm{Ar}$	$f(\varepsilon)$
Electron-collision excitation and de-excitation		
R2, 3	$e + \mathrm{Ar} \leftrightarrow e + \mathrm{Ar}^*$	$f(\varepsilon)$
R4, 5	$e + \mathrm{Ar} \leftrightarrow e + \mathrm{Ar}_r^*$	$f(\varepsilon)$
R6, 7	$e + \mathrm{Ar} \leftrightarrow e + \mathrm{Ar}^{**}$	$f(\varepsilon)$
R8, 9	$e + \mathrm{Ar}^* \leftrightarrow e + \mathrm{Ar}^{**}$	$f(\varepsilon)$
R10 (remainder of total excitation, $\varepsilon = 13.91$ eV)	$e + \mathrm{Ar} \rightarrow e + \mathrm{Ar}$	$f(\varepsilon)$
R11	$e + \mathrm{Ar}_2^* \rightarrow e + \mathrm{Ar}_2^{**}$	$f(\varepsilon)$
Electron-collision ionization		
R12	$e + \mathrm{Ar} \rightarrow 2e + \mathrm{Ar}^+$	$f(\varepsilon)$
R13	$e + \mathrm{Ar}^* \rightarrow 2e + \mathrm{Ar}^+$	$f(\varepsilon)$
R14	$e + \mathrm{Ar}_r^* \rightarrow 2e + \mathrm{Ar}^+$	$f(\varepsilon)$
R15	$e + \mathrm{Ar}^{**} \rightarrow 2e + \mathrm{Ar}^+$	$f(\varepsilon)$
Electron–ion recombination		
R16	$e + \mathrm{Ar}_2^+ \rightarrow \mathrm{Ar} + \mathrm{Ar}^{**}$	$1.1 \times 10^{-7} T_e^{-1/2}$ $\mathrm{cm^3 s^{-1}}$
R17	$e + \mathrm{Ar}_3^+ \rightarrow 2\mathrm{Ar} + \mathrm{Ar}^{**}$	$2.1 \times 10^{-7} T_e^{-1/2}$ $\mathrm{cm^3 s^{-1}}$
Charge-transfer reaction		
R18	$2\mathrm{Ar} + \mathrm{Ar}^+ \rightarrow \mathrm{Ar} + \mathrm{Ar}_2^+$	2.5×10^{-31} $\mathrm{cm^6 s^{-1}}$
R19	$2\mathrm{Ar} + \mathrm{Ar}_2^+ \rightarrow \mathrm{Ar} + \mathrm{Ar}_3^+$	6×10^{-32} $\mathrm{cm^6 s^{-1}}$
R20	$\mathrm{Ar} + \mathrm{Ar}_3^+ \rightarrow 2\mathrm{Ar} + \mathrm{Ar}_2^+$	10^{-12} $\mathrm{cm^3 s^{-1}}$
Quenching		
R21	$\mathrm{Ar} + \mathrm{Ar}^{**} \rightarrow \mathrm{Ar} + \mathrm{Ar}^*$	4×10^{-11} $\mathrm{cm^3 s^{-1}}$
R22	$\mathrm{Ar} + \mathrm{Ar}^* \rightarrow \mathrm{Ar} + \mathrm{Ar}_r^*$	2×10^{-7} $\mathrm{cm^3 s^{-1}}$
R23	$\mathrm{Ar} + \mathrm{Ar}_2^{**} \rightarrow 2\mathrm{Ar} + \mathrm{Ar}^*$	10^{-12} $\mathrm{cm^3 s^{-1}}$
R24	$2\mathrm{Ar} + \mathrm{Ar}^* \rightarrow \mathrm{Ar} + \mathrm{Ar}_2^*$	10^{-32} $\mathrm{cm^6 s^{-1}}$
Chemo-ionization processes		
R25	$2\mathrm{Ar}^* \rightarrow \mathrm{Ar} + \mathrm{Ar}^+ + e$	1.2×10^{-9} $\mathrm{cm^3 s^{-1}}$
R26	$2\mathrm{Ar}^{**} \rightarrow \mathrm{Ar} + \mathrm{Ar}^+ + e$	1.2×10^{-9} $\mathrm{cm^3 s^{-1}}$
R27	$2\mathrm{Ar}_r^* \rightarrow \mathrm{Ar} + \mathrm{Ar}^+ + e$	1.2×10^{-9} $\mathrm{cm^3 s^{-1}}$
R28	$\mathrm{Ar}^* + \mathrm{Ar}^{**} \rightarrow \mathrm{Ar} + \mathrm{Ar}^+ + e$	1.2×10^{-9} $\mathrm{cm^3 s^{-1}}$
R29	$\mathrm{Ar}^* + \mathrm{Ar}_r^* \rightarrow \mathrm{Ar} + \mathrm{Ar}^+ + e$	1.2×10^{-9} $\mathrm{cm^3 s^{-1}}$
R30	$\mathrm{Ar}^* + \mathrm{Ar}_2^* \rightarrow 2\mathrm{Ar} + \mathrm{Ar}^+ + e$	1.2×10^{-9} $\mathrm{cm^3 s^{-1}}$
R31	$\mathrm{Ar}_r^* + \mathrm{Ar}_2^* \rightarrow 2\mathrm{Ar} + \mathrm{Ar}^+ + e$	1.2×10^{-9} $\mathrm{cm^3 s^{-1}}$
R32	$2\mathrm{Ar}_2^* \rightarrow 2\mathrm{Ar} + \mathrm{Ar}_2^+ + e$	1.2×10^{-9} $\mathrm{cm^3 s^{-1}}$
Radiative processes		
R33	$\mathrm{Ar}_2^* \rightarrow 2\mathrm{Ar} + h\nu$	3.8×10^6 $\mathrm{s^{-1}}$
R34	$\mathrm{Ar}_2^{**} \rightarrow \mathrm{Ar} + \mathrm{Ar}^* + h\nu$	10^{11} $\mathrm{s^{-1}}$
R35	$\mathrm{Ar}^{**} \rightarrow \mathrm{Ar}^* + h\nu$	3×10^7 $\mathrm{s^{-1}}$
R36	$\mathrm{Ar}_r^* \rightarrow \mathrm{Ar} + h\nu$	3.33×10^5 $\mathrm{s^{-1}}$

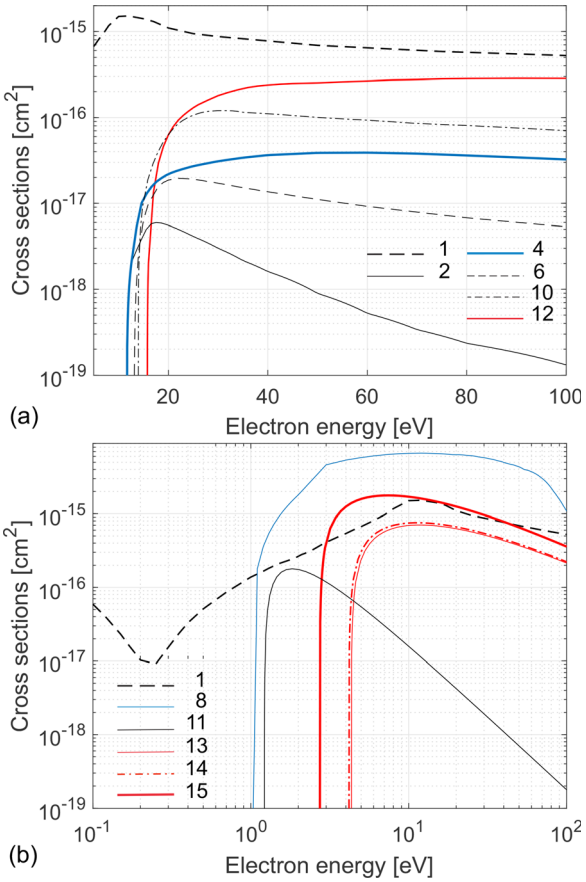

FIG. 2. Electron cross sections for (a) elastic, direct ionization, excitation collisions, and (b) stepwise ionization and other collisions in the plasma-chemical model for DBD in argon, used in the model. The labels correspond to indices of corresponding reactions in Table II.

power deposition (c) obtained as functions of the applied voltage amplitude V_0, varied over the range from 0.8 to 4 kV, are shown in Fig. 3. Calculations are carried out for the applied AC field frequencies $f = 20$, 45, 70, 95, and 120 kHz. Other parameters are defined as in Sec. C. The period average dissipated power is calculated from

$$\langle P_\mathrm{d} \rangle = \frac{1}{T} \int_0^T I(t) V_\mathrm{g}(t) dt,$$

where I is the discharge current and V_g is the voltage over the discharge gap, the efficiency from

$$\eta = \frac{\langle P_\mathrm{d} \rangle}{I_\mathrm{rms}\, V_\mathrm{rms}},$$

where the RMS values are obtained from

$$A_\mathrm{rms} = \left[\frac{1}{T} \int_0^T A^2(t) dt \right]^{\frac{1}{2}}$$

and $V_\mathrm{rms} = V_0/\sqrt{2}$.

TABLE III. Boundary conditions at the edges of the discharge gap.

Electron flux	$\hat{\mathbf{n}} \cdot \mathbf{\Gamma}_e = \frac{1}{2} \nu_e n_e - \sum_i \gamma_i (\hat{\mathbf{n}} \cdot \mathbf{\Gamma}_i)$
Ion flux (species 7–9 in Table I)	$\hat{\mathbf{n}} \cdot \mathbf{\Gamma}_i = \frac{1}{4} \xi_i \nu_i n_i + a n_i \mu_i (\hat{\mathbf{n}} \cdot \mathbf{E})$
Effective excited and excimer species flux (2–6 in Table I)	$\hat{\mathbf{n}} \cdot \mathbf{\Gamma}_h = \frac{1}{2} \nu_h n_h$
Electron energy flux	$\hat{\mathbf{n}} \cdot \mathbf{\Gamma}_\varepsilon = \frac{5}{6} \nu_e n_\varepsilon - \sum_i \gamma_i \varepsilon_i (\hat{\mathbf{n}} \cdot \mathbf{\Gamma}_i)$
Surface charge density	$\sigma = (\varepsilon_r \varepsilon_0 \mathbf{E}_d - \varepsilon_0 \mathbf{E}_g) \cdot \hat{\mathbf{n}}, \frac{\partial \sigma}{\partial t} = \mathbf{J}_g \cdot \hat{\mathbf{n}}$
Background gas temperature	$T_g = 300$ K

In order to convert the computed current densities to the discharge currents I, the current densities were integrated over the discharge tube volume of the height equal to the external electrode wrap 9 cm, in accordance with the discharge cell design in Ref. 19, assuming uniformity of the current density in the axial direction.

Note that Fig. 3 includes results obtained from models based on the Maxwellian eedf (dash lines) and more realistic eedf (solid lines) computed from the relevant electron Boltzmann equation. It is worth noting that the current $I_{\rm rms}$ and dissipated power $\langle P_{\rm d} \rangle$ obtained from the model with the Maxwellian eedf exhibit a linear dependence on the voltage V_0 [see Figs. 3(a) and 3(b)], such that the gas breakdown process seems to be overlooked. Results obtained from the model with more realistic eedf clearly reveal the discharge breakdown voltage, whose value is about 1.8 kV and slowly increases with decrease in the field frequency f. The reason for this behavior is related to the fact that in the case of the Maxwellian eedf, the plasma does not completely decay by the beginning of the next period, i.e., the discharge gap remains a highly conductive medium. In this case, Ohm's law is fulfilled for the electric circuit and the magnitude of the electric current follows the voltage. In turn, for a non-Maxwellian eedf obtained from the Boltzmann equation, the plasma decays by the beginning of a new period, i.e., becomes an insulator (non-conductive medium). Therefore, each time the discharge process starts anew: first, with increasing voltage, gas breakdown occurs, and only after the formation of plasma is the proportionality of current and voltage observed.

As can be observed from Fig. 3(a), for larger values of V_0 (and, equivalently, for larger discharge currents), $I_{\rm rms}$ profiles derived from these two models behave similarly as linear functions of the voltage V_0, where the current profiles corresponding to the same values of f are close to one another. Shapes of the profiles $\langle P_{\rm d} \rangle$ vs V_0 obtained from the model with more adequate eedf also became linear with respect to larger values of V_0 [see Fig. 3(b)]; however, the profiles corresponding to the different models are located distant from one another.

Significant discrepancy in the solution profiles of efficiency η plotted against voltage V_0, obtained from these two models, can be seen from Fig. 3(c). Note that profiles from the model with the Maxwellian eedf are closely spaced together, independent of field

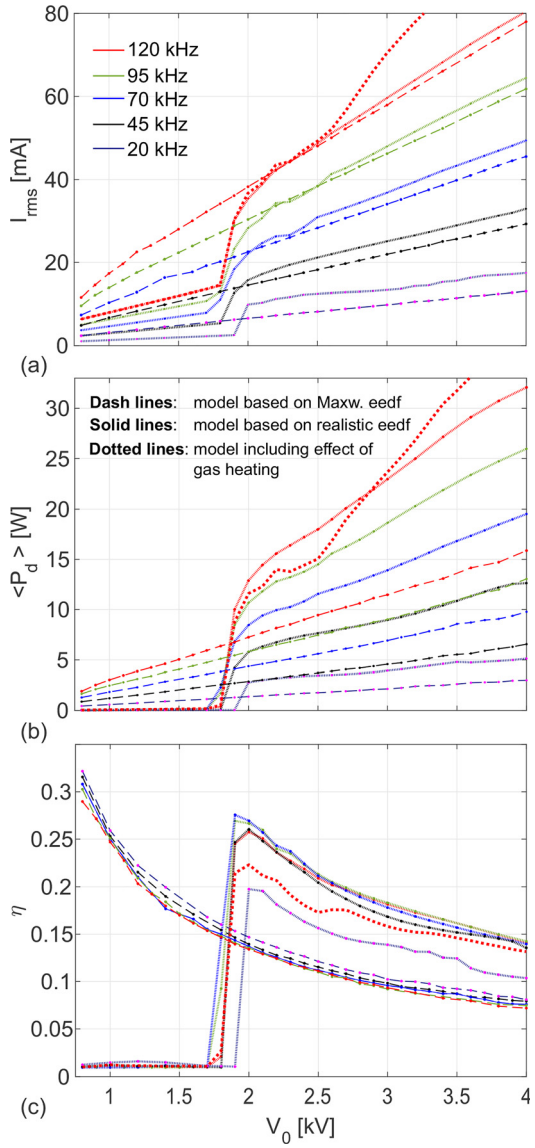

FIG. 3. (a) RMS of the discharge current $I_{\rm rms}$, (b) period average dissipated power $\langle P_{\rm dis} \rangle$, and (c) efficiency of the power deposition η vs amplitude V_0 of the applied field. $p = 1$ atm, $d = 0.825$ mm, $\varepsilon_r = 4$, $\gamma = 0.1$.

frequency f from the considered range of values. Profiles for η derived from the model with more adequate eedf are also sufficiently close to one another, for all frequencies, except at the smallest frequency $f = 20$ kHz, where the corresponding profile falls far apart from the others. Local maximum of efficiency η obtained from this model is about 0.25; corresponding values of η are greater than those from the model with the Maxwellian eedf [see Fig. 3(c)].

Note that Fig. 3 also includes solution profiles (for frequency $f = 120$ kHz) obtained from the model based on realistic eedf but with heating of the background gas taken into account (red dotted line). When implementing this model, in order to speed up the calculations, the explicit time derivative of the gas temperature in the heat

conduction equation given by Eq. (5) was eliminated. This is a reasonable approximation due to significant difference in the time scales associated with the thermal conductivity compared to that for the plasma processes in the discharge. Indeed, for the present discharge conditions, the characteristic time scale of thermal heat transfer is about three orders of magnitude greater than the period of field oscillations, and also several orders of magnitude greater than characteristic time scales of the plasma-chemical processes.[19]

As can be observed [see panels (a) and (b) in Fig. 3], for relatively small values of voltage V_0 (and, equivalently, small discharge currents), the profiles of I_{rms} and $\langle P_d \rangle$ against voltage V_0 behave similarly to the corresponding profiles from the model where gas heating is ignored. However, these profiles diverge from their counterparts for larger values of V_0.

In the following analysis, the model based on the realistic eedf computed from the relevant electron Boltzmann equation is employed. Heating of the gas is ignored in the model. In fact, this model has been verified and validated in Ref. 19. Indeed, combined numerical and experimental studies in Ref. 19 have shown that taking account of the energy losses due to gas heating does not provide any benefit in terms of better agreement with the experimental data and that the gas heating can be safely neglected.

In Fig. 4, the same discharge characteristics from Fig. 3, i.e., RMS of the discharge current I_{rms} (a), the average dissipated power $\langle P_d \rangle$ (b), and efficiency η of the power deposition (c), are depicted on the plane spanned by the voltage amplitude V_0 and frequency f of the applied field. As can be seen from panels (a) and (b) in this figure, the discharge current I_{rms} and dissipated power $\langle P_d \rangle$ increase with voltage V_0 and frequency f of the field. Similar trends for the dissipated power have been observed previously for parallel-plate and coaxial DBDs.[13,14,16] Note that the efficiency η of power deposition is weakly dependent on the frequency f [see panel (c)]. Power deposition is more effective in a narrow region of the parameter space [with efficiency about $\eta = 0.25$, see Fig. 4 (c)] extending from 1900 to 2200 V along the voltage axis and from 40 to 120 kHz along the frequency axis, where this region is wider about $f = 80$ kHz.

B. Effect of the dielectric constant

Figure 5 illustrates results of the parametric study of the RMS of the discharge current I_{rms} (first column), the period average value of the dissipated power $\langle P_d \rangle$ (second column), and the efficiency η of power deposition (third column) in the parameter space spanned by the applied voltage amplitude V_0 and the barrier dielectric constant ε_r, ranging from 0.8 to 4 kV and from 4 to 8, respectively. Analysis is performed for the field frequencies $f = 20$ (a), 45 (b), 70 (c), 95 (d), and 120 kHz (e). As can be observed, for each of these frequencies, the discharge current I_{rms} and dissipated power $\langle P_d \rangle$ increase gradually with increase in ε_r and voltage V_0, except at $f = 20$ kHz, where I_{rms} increased with V_0 non-monotonically. Moreover, as can be seen from the first two columns of Fig. 5, the values of the discharge current I_{rms} and dissipated power $\langle P_d \rangle$ increase with increasing frequency f. This trend is consistent with the observations in Ref. 13 for the coaxial DBD in helium. It is interesting to observe from the third column in Fig. 5 that the maximum efficiency of the power deposition η of about 0.25 is the same for all values of field frequencies f ranging from 20 to 120 kHz. Moreover, it occurs in nearly the same region in the plane of parameters V_0 and ε_r, where the voltage amplitudes are about 2000 V, closer to the left end, $\varepsilon_r = 4$, of the interval for the barrier dielectric constant.

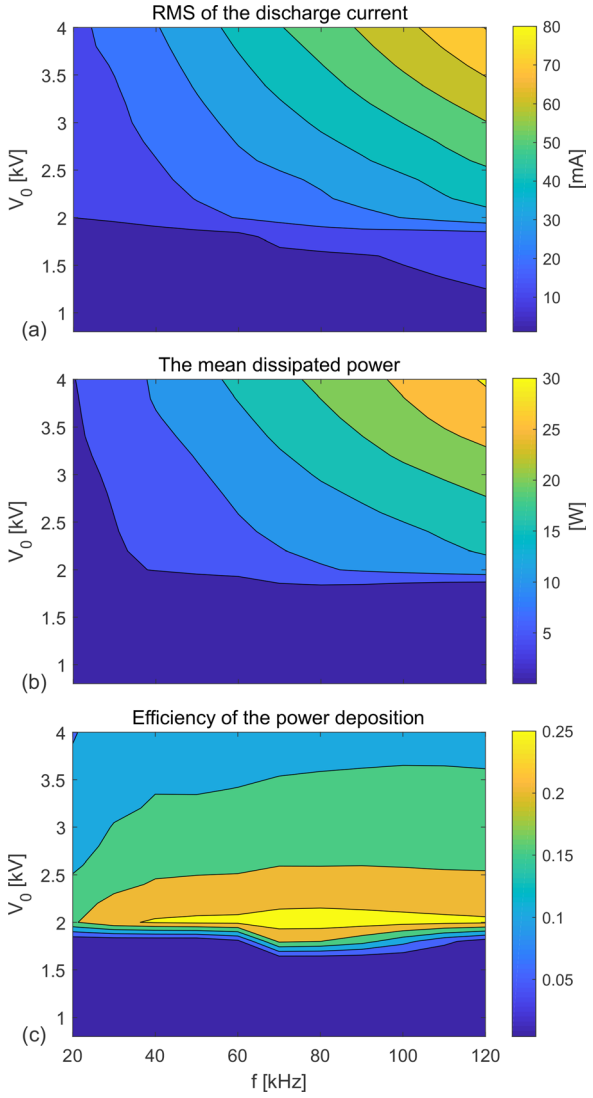

FIG. 4. (a) RMS of the discharge current I_{rms} (in mA), (b) period average of the dissipated power $\langle P_{dis} \rangle$ (in W), and (c) efficiency of the power deposition η vs applied voltage amplitude V_0 and field frequency f. $p = 1$ atm, $d = 0.825$ mm, $\varepsilon_r = 4$, $\gamma = 0.1$.

C. Effect of the gas gap width

Figure 6 shows results of the parametric study of the discharge characteristics from Figs. 4 and 5, which are the RMS values of the discharge current I_{rms}, the period average value of the dissipated power $\langle P_d \rangle$, and efficiency η of the power deposition. The parameter space is spanned by the applied voltage amplitude V_0 and the gas gap width d, which vary from 0.8 to 4 kV and from 0.5 to 4 mm, respectively. The range 20 (a), 45 (b), 70 (c), 95 (d), and 120 kHz (e) for the applied field frequencies f is explored. As can be observed, the dependence of the

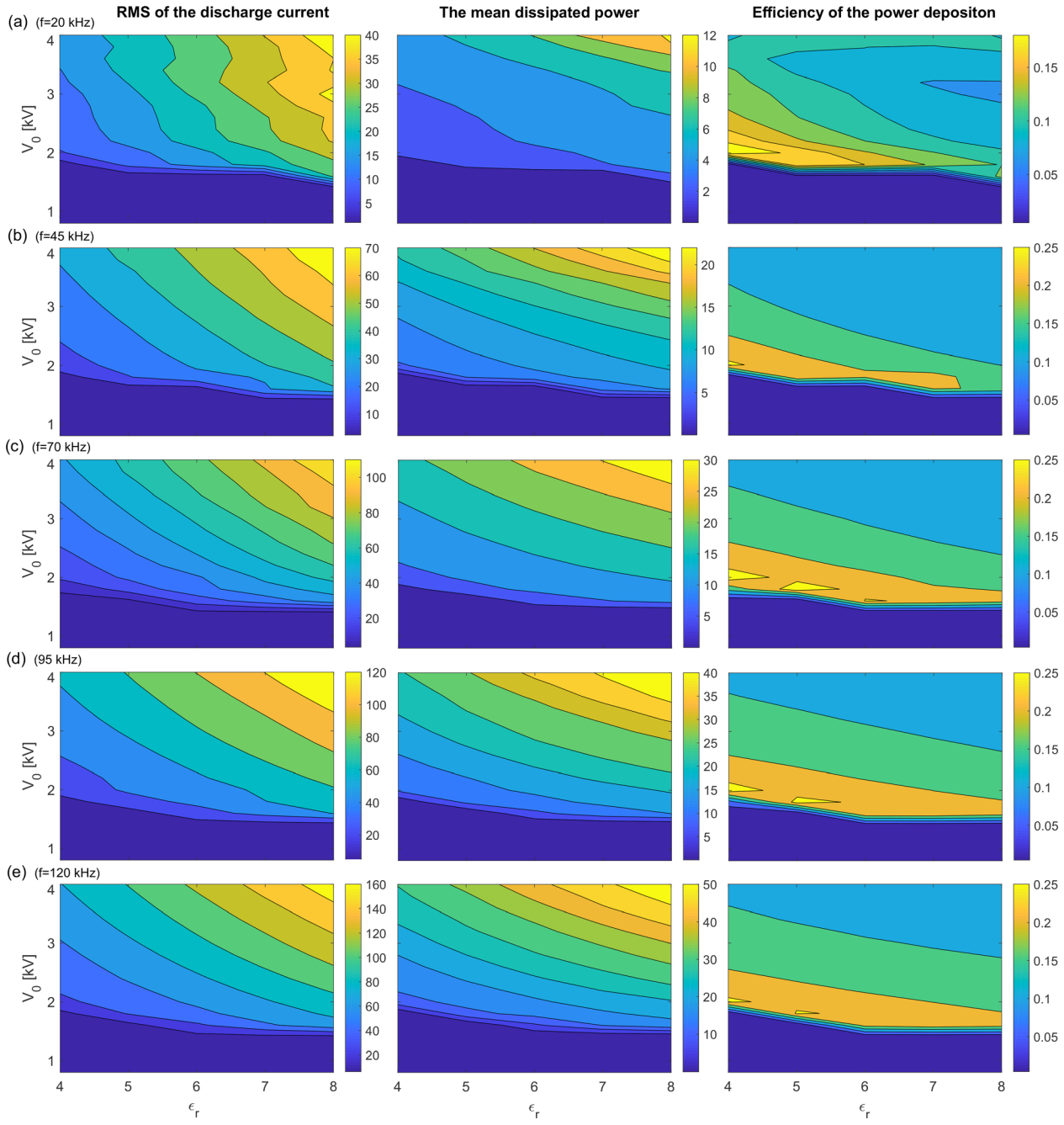

FIG. 5. RMS of the discharge current I_{rms} (in mA), period average dissipated power $\langle P_{dis}\rangle$ (in W), and efficiency of the power deposition η vs amplitude V_0 of the applied field and the dielectric constant ε_r. The field frequencies f are 20 kHZ (a), 45 kHZ (b), 70 kHZ (c), 95 kHZ (d), and 120 kHZ (e). $p = 1$ atm, $d = 0.825$ mm, $\gamma = 0.1$.

discharge current $I_{\rm rms}$, the dissipated power $\langle P_{\rm d}\rangle$, and efficiency η on the voltage V_0 and the gap width d, in principle, is similar, for the field frequencies f from the considered range of values. The discharge current $I_{\rm rms}$ and dissipated power $\langle P_{\rm d}\rangle$ increase monotonically with increasing voltage V_0, and also increase with the frequency f. However, these characteristics depend non-linearly on the gas gap d. Note that $I_{\rm rms}$ and $\langle P_{\rm d}\rangle$ reach their peaks for a gap width about 3 mm, in the region closer to the right end of the interval for d. As can be seen from the third column in Fig. 6, the maximum efficiency of power deposition η changes from about 0.15 for $f = 20$ kHz to 0.20 for $f = 45$ kHz, and 0.25 for greater values of the frequency f. These peaks are attained in nearly the same region in the plane of the voltage V_0 and the gas

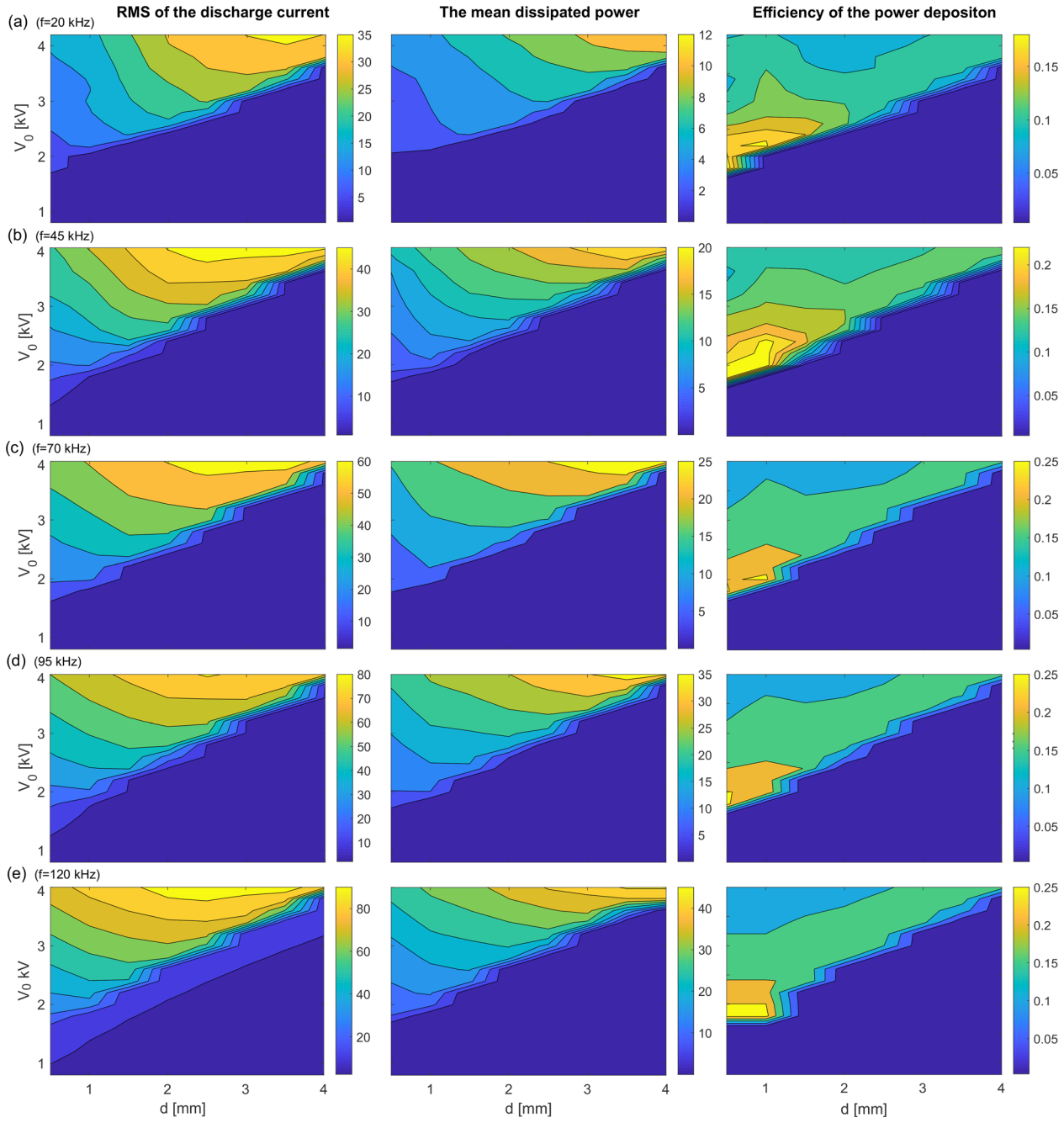

FIG. 6. RMS of the discharge current I_{rms} (in mA), period average dissipated power $\langle P_{dis} \rangle$ (in W), and efficiency of the power deposition η vs amplitude V_0 of the applied field and gas gap width d. The field frequencies f are 20 kHZ (a), 45 kHZ (b), 70 kHZ (c), 95 kHZ (d), and 120 kHZ (e). $p = 1$ atm, $\varepsilon_r = 4$, $\gamma = 0.1$.

gap width d, where the voltage amplitudes are about 2000 V, closer to the left end of the interval for d.

IV. CONCLUSIONS

Parametric study of the coaxial DBD in atmospheric pressure argon is carried out. The numerical model is similar to that employed in our previous work,[19] where it was verified by superimposing relevant data obtained from the simulations and measurements of the barrier discharge characteristics. It is spatially one-dimensional, based on the drift-diffusion equations for particle fluxes. The electron kinetic coefficients (the electron transport coefficients as well as the rate constants of the electron-induced elementary processes) are defined as functions of

electron mean energy, derived from the solution of the Boltzmann equation for the eedf. The results of the modeling approaches, where

- the electron kinetic coefficients are computed under the assumption that the eedf is Maxwellian, and
- the energy loss due to the background gas heating is taken into account,

were also demonstrated.

A parametric study of the barrier discharge integral characteristics, i.e., the root mean square of the discharge current, the period average dissipated power, and the efficiency of the power deposition is performed. The parameter space is spanned by the voltage amplitude ($0.8 \leq V_0 \leq 4$ kV) and frequency ($20 \leq f \leq 120$ kHz) of the applied AC field, the barrier dielectric constant ($4 \leq \varepsilon_r \leq 8$), and the gas gap width ($0.5 \leq d \leq 4$ mm).

The observations described in this work are in good agreement with the previously reported literature for both parallel-plate and cylindrical DBD geometries. The time averaged discharge current and dissipated power are shown to increase monotonically with an increase in the applied voltage amplitude, field frequency, and relative permittivity of the barrier, and an increase non-monotonically with the increase in the gas gap width. Calculations reveal that the efficiency of power deposition peaks in the region of parameter space about voltage amplitude $V_0 = 2$ kV, about the left ends of the intervals for the gap width d and the dielectric constant ε_r, practically independent of the field frequency f from the considered set of values.

ACKNOWLEDGMENTS

This work was supported in part by the research Grant No. 11775062 from the National Natural Science Foundation of China (NSFC) and by the research Grant No. 3191899 from the Scientific and Technical Research Council of Turkey (TUBITAK).

AUTHOR DECLARATIONS

Conflict of Interest

The authors have no conflicts to disclose.

DATA AVAILABILITY

The data that support the findings of this study are available within the article.

REFERENCES

[1]U. Kogelschatz, Plasma Chem. Plasma Process. **23**, 1–46 (2003).
[2]A. A. Fridman and G. G. Friedman, *Plasma Medicine* (John Wiley & Sons, Chichester, UK, 2013).
[3]G. Park, S. Park, M. Choi, I. Koo, J. Byun, J. Hong, J. Sim, G. Collins, and J. Lee, Plasma Sources Sci. Technol. **21**, 043001 (2012).
[4]D. Li, V. Rohani, F. Fabry, A. P. Ramaswamy, M. Sennour, and L. Fulcheri, Appl. Catal. B: Environ. **261**, 118228 (2020).
[5]U. Kogelschatz, IEEE Trans. Plasma Sci. **30**, 1400–1408 (2002).
[6]F. Massines, N. Gherardi, N. Naudé, and P. Ségur, Eur. Phys. J. Appl. Phys. **47**, 22805 (2009).
[7]M. Becker, T. Hoder, R. Brandenburg, and D. Loffhagen, J. Phys. D: Appl. Phys. **46**, 355203 (2013).
[8]R. Brandenburg, Plasma Sources Sci. Technol. **26**, 053001 (2017).
[9]B. Chen, Z. Tan, and X. Song, IEEE Trans. Plasma Sci. **40**, 1103–1109 (2012).
[10]Q. Wang, J. Sun, and D. Wang, Phys. Plasmas **18**, 103504 (2011).
[11]G. Pan, Z. Tan, J. Pan, X. Wang, and C. Shan, Phys. Plasmas **23**, 043508 (2016).
[12]X. Li, N. Zhao, T. Fang, Z. Liu, L. Li, and L. Dong, Plasma Sources Sci. Technol. **17**, 015017 (2008).
[13]S. Gadkari and S. Gu, Phys. Plasmas **24**, 053517 (2017).
[14]D. Petrović, T. Martens, J. Van Dijk, W. Brok, and A. Bogaerts, J. Phys. D: Appl. Phys. **42**, 205206 (2009).
[15]U. Pal, A. Sharma, J. Soni, S. Kr, H. Khatun, M. Kumar, B. Meena, M. Tyagi, B. Lee, M. Iberler *et al.*, J. Phys. D: Appl. Phys. **42**, 045213 (2009).
[16]R. Valdivia-Barrientos, J. Pacheco-Sotelo, M. Pacheco-Pacheco, J. Benítez-Read, and R. López-Callejas, Plasma Sources Sci. Technol. **15**, 237 (2006).
[17]A. Bogaerts, T. Kozák, K. Van Laer, and R. Snoeckx, Faraday Discuss. **183**, 217–232 (2015).
[18]A. Bogaerts, A. Berthelot, S. Heijkers, S. Kolev, R. Snoeckx, S. Sun, G. Trenchev, K. Van Laer, and W. Wang, Plasma Sources Sci. Technol. **26**, 063001 (2017).
[19]H. Li, C. Yuan, A. Kudryavtsev, A. Astafiev, E. Bogdanov, T. Y. Katircioglu, and I. Rafatov, J. Appl. Phys. **129**, 153305 (2021).
[20]G. Hagelaar and L. Pitchford, Plasma Sources Sci. Technol. **14**, 722 (2005).
[21]I. Rafatov, E. A. Bogdanov, and A. A. Kudryavtsev, Phys. Plasmas **19**, 033502 (2012).
[22]See http://www.comsol.com for "COMSOL MULTIPHYSICS v. 5.6 (Stockholm: COMSOL AB)."
[23]E. Bogdanov, A. Kudryavtsev, and A. Chirtsov, Tech. Phys. **56**, 55–60 (2011).
[24]G. Hagelaar, F. De Hoog, and G. Kroesen, Phys. Rev. E **62**, 1452 (2000).
[25]COMSOL MULTIPHYSICS v. 5.6 2020 Plasma Module User's Guide (Stockholm: COMSOL AB, 2020).